ARTICLE

Magnetocaloric effect observations near room temperature in few-layered chromium telluride (Cr_2Te_3)

Received 00th January 20xx,
Accepted 00th January 20xx

DOI: 10.1039/x0xx00000x

Nishant Tiwari[a] ‡, Chinmayee Chowde Gowda[b] ‡, Subhendu Mishra[c], Prafull Pandey[d], Saikat Talapatra[e], Varun Chaudhary[f], Abhishek K. Singh[c*] and Chandra Sekhar Tiwary[a,b*]

Transition metal telluride compositions are explored extensively for their unique magnetic behavior. Few-layered chromium telluride (Cr_2Te_3) exhibited a near-room-temperature phase transition, where the material can be effectively used in applications such as magnetic refrigeration. Compared to existing magnetocaloric materials, Heusler alloys, and rare-earth-based alloys, the large-scale synthesis of mechanically exfoliated Cr_2Te_3 involves less complexity, resulting in a stable composition. Compared to existing tellurides, Cr_2Te_3 exhibited a large change in magnetic entropy *($|\Delta S_M|$)* of 1.88 J/kg-K at a magnetic field of 4 *T*. The refrigeration capacity *(RC)* of ~ 82 J/kg was determined from the change in magnetic entropy versus temperature curve. The results were comparable with the existing Cr-compounds. First-principles density functional theory (DFT) confirmed the magnetic properties of Cr_2Te_3, including a near-room-temperature Curie temperature, T_C, consistent with experimental results. Structural transition was also observed using first principles DFT, which is responsible for the magnetic behavior.

Introduction

Recently, transition metal chalcogenides (TMDCs) have gained interest for their excellent magnetic properties and potential applications in magnetocaloric, spintronics, topological, and anomalous Hall Effect. Telluride compositions, varying from bulk to lower dimensions, have received significant attention due to their structural effects on magnetic property variation and potential applications in various fields [1–3]. The van der Waals ferromagnetic properties exhibited especially by Cr-based chalcogenides have sparked interest in reduced-dimensional magnetic systems [4–10]. A few binary Cr-Te compositions studied in this regard are Cr_4Te_5[4], Cr_5Te_8 [5–7] and Cr_2Te_3 [11]. These compounds are reported to be ferromagnets, with various magnetic phase transition temperatures ranging from 160 to 340 K depending on Cr concentration. Recently, there have been ample studies on Cr_2Te_3, where the studies indicated that the magnetic phase transition temperature can also be tuned close to room temperature, depending on the processing conditions [12–15].

One such area of application for near RT magnetic phase transition is in the fields of non-gaseous magnetic refrigeration. Magnetic refrigeration, which works on the magnetocaloric effect (MCE) of magnetic materials, has reconstituted the refrigeration industry due to its energy-efficient and sustainable approach [16,17]. In this solid-state refrigeration technique, the change in magnetic entropy and therefore in temperature of a magnetic material under an external magnetic field in adiabatic conditions is observed. Different types of magnetocaloric materials (MCM) can be used for magnetic refrigeration, exhibiting a temperature drop upon the application of external magnetic fields. MCE was first reported in gadolinium (Gd) [18], and since then, numerous rare-earth-based alloys have been explored for their magnetocaloric properties [18,19]. Apart from rare-earth-based alloys, Heusler alloys are also known for their giant magnetocaloric effect (GMCE) [20–22].

Many TMDCs with first-order ferromagnetic to paramagnetic transitions exhibit MCE. Few telluride compositions such as Nd_3Te_4 have also been explored for their enhanced magnetocaloric properties [23]. MCE is quantified by the isothermal entropy change ($|\Delta S_M|$) or adiabatic temperature change (ΔT_{ad}) with respect to the applied magnetic field. Both parameters ($|\Delta S_M|$, ΔT_{ad}) show their maximum value around the transition temperature. The development of advanced MCMs at room temperature has become an important research area as it plays a significant role in improving the efficiency of magnetic refrigeration and has an economic impact on commercialization[24,25]. A few recent studies on single-crystal chromium tellurides displaying high entropy changes near T_C [11,26] have prompted studies on the unique magnetic properties exhibited by Cr_2Te_3. Single crystals, which were grown using chemical vapor deposition, showed that, when the magnetic fields were applied parallel to the *c*-axis, a maximum change in magnetic entropy ($|\Delta S_M|$) of 2.08 J kg^{-1} K^{-1} was estimated around the T_C of 170 K upon application of high magnetic fields of 6 *T* [26]. In another study, single-crystal Cr_2Te_3 samples were reported with $|\Delta S_M|$ of 4.5 J kg^{-1} K^{-1} at 9 *T* [11]. The reported studies involve growing Cr_2Te_3 in pristine conditions, which restricts large-scale utilization of the material for a wide range of device applications. A recent theoretical paper on exploring CrX_3 (X= F, Cl, Br, and I) and $GdSi_2$ monolayers showed that

[a]Department of Metallurgy and Materials Engineering, Indian Institute of Technology Kharagpur, West Bengal - 721302, India
[b]School of Nano Science and Technology, Indian Institute of Technology Kharagpur, West Bengal – 721302, India
[c]Materials Research Centre, Indian Institute of Science, Bengaluru, Karnataka – 560012, India
[d]Department of Materials Engineering, Indian Institute of Technology Gandhinagar, Gujarat – 382355, India
[e]School of Physics and Applied Physics, Southern Illinois University, Carbondale, IL 62901, USA
[f]Industrial and Materials Science, Chalmers University of Technology, SE-41296 Gothenburg, Sweden

Please do not adjust margins

because of their stronger critical fluctuations and weaker interlayer vdW interactions, 2D magnets have a lower T_C and a quicker transition of magnetisation with temperature close to T_C [27]. These are helpful in achieving a greater ΔS_M and suggest that a lesser external magnetic field may be sufficient to drive 2D magnetocaloric. A recent work showed a multiscale simulation model of Cr-based compounds resulting in a giant magnetocaloric effect in these two-dimensional (2D) materials [4,28]. A substantial isothermal entropy change -ΔS_M of 12.3 J/kgK and adiabatic temperature change of 2.3 K during magnetic phase transition [28].

In the present study, we explore the magnetocaloric properties of few-layered Cr_2Te_3 synthesized using an easily scalable melting process followed by mechanical exfoliation. As Cr_2Te_3 exhibits a second-order magnetic phase transition, which provides the change in magnetic entropy over broad temperature ranges with no magnetic or thermal hysteresis, the material is best suited for magnetocaloric applications. The layered Cr_2Te_3 sample was thoroughly analyzed for its structural, magnetic, and magnetocaloric properties. The material exhibits a wide range of applications spanning from magnetic units [4,26,29] to nanogenerators [30]. Temperature-dependent magnetization (M-T) measurements show ferromagnetic to paramagnetic transition (T_C) towards near room temperature in the range of 304 - 308 K. To verify our experimental findings, density functional theory (DFT) calculations were also performed to explore the relationship between experimental and calculated T_C values of Cr_2Te_3. DFT calculations were performed to simulate structural changes in the investigated alloys at different temperatures using *ab-initio* Molecular Dynamics (AIMD). As a proof-of-concept, the first phase of the magnetic cycle during the magnetocaloric refrigeration was visualized with the help of a thermal imaging camera. Samples were analysed for their magnetic behaviour with and without exposure to an external magnetic source.

Material and methods

Material synthesis

Chromium telluride was prepared using the induction melting method, due to the large temperature variation between Cr and Te melting points. This method can be used to produce polycrystalline Cr_2Te_3 samples on a large scale with less sophisticated fabrication techniques. Stochiometric amounts of the elements are sealed in a quartz tube with Argon backfilling before melting [31]. The heating temperature of the sample was kept below the boiling point of Te (950 °C), and an increased holding time up to 4 hours. The temperature is measured with the help of a thermocouple, as shown in **Figure S1,** to ensure constant temperature throughout the holding time. This period results in time-dependent diffusion of elements. The outside temperature of the quartz tube may vary ± 2 °C. Further, to obtain a homogeneous alloy, the as-cast sample is cooled down to room temperature in the melting unit and then annealed. The as-cast sample is cut into small chunks using a diamond cutter. The as-cast is sealed again in a quartz tube with backfilling of Ar atmosphere for annealing at 1173 K for 100 hours. The samples were brought to room temperature gradually in the furnace before using them for further characterization. Isopropyl alcohol (IPA) was used as the solvent medium in a mechanical exfoliation process to produce the exfoliated flakes. For eight hours, a probe sonicator operating at a frequency of 30 kHz and a pulse rate of 10 s was employed. After letting the suspension settle for a full day, the supernatant was gathered and dried for further use. Induction or arc melting enables control of vapor pressures and effective homogenization. Previous studies from our group have used melting and exfoliation techniques to support this approach [32–37]. The alloys achieved uniform composition through thermal annealing under vacuum or argon, ensuring stoichiometric balance. Comprehensive characterization (XRD, SEM, EDX, XPS, and STEM) confirmed phase purity. Similar synthesis strategies have been applied to 2D materials [38–40], offering advantages for large-scale telluride production in multifunctional device applications.

Characterization tools

The compositions of the prepared sample were confirmed using energy dispersive X-ray spectroscopy (EDS). The X-ray diffraction pattern is collected at room temperature using a Cu-K_α target in Bruker D8 Advance diffractometer. The microstructure features were analyzed using a ZEISS GEMINI 600 field-emission scanning electron microscope (FE-SEM). Atomic force microscopy (AFM) was carried out utilizing an Agilent Technologies Model No. 5500. On a monocrystalline silicon substrate, the sample was deposited using the drop deposition technique. The structural characterization was further probed using a high-angle annular dark-field scanning transmission electron microscopy (HAADF-STEM) operated at 300 kV. The magnetic characterization of the samples is performed using the SQUID (Superconducting quantum interference devices) module of an MPMS (Quantum Design, USA). The magnetization versus temperature (M-T) behaviour of the samples was analyzed in conditions such as Field warming (FC) and Field cooling (FC) protocols at a magnetic field of 1 Tesla *(T)*. Furthermore, M-H isotherms were measured across the transition temperature *(T_C)* by varying the field from 0 - 4 *T* to calculate the change in magnetic entropy *($|\Delta S_M|$)*.

Device fabrication and Thermal Imaging

A device was fabricated using exfoliated Cr_2Te_3 powders, which were quite brittle in nature, making it easier for exfoliation. The powders were mixed with acetone to form a paste and then moulded into a thin layer with an approximate thickness of 0.5 mm. The device was then heated at 60 °C to eliminate the solvent and any moisture content from the material. The refrigerant material device was subjected to a neodymium iron boron (NdFeB) magnet with a magnetic field of 2000 G. We used a thermal imaging setup to observe the heat fluctuations during the heating and cooling cycle. The thermal imaging camera (Optris PI 640i) with a temperature range -20 °C to 900 °C, spectral range: 8 to 14 µm, frame rate: up to 125 Hz. The sensors in the thermal camera are of thermal sensitivity of 40 mK. The temperature range of -35 °C (238 K) to 40 °C (313 K) was measured during the heating and cooling. The thermal imaging setup uses an uncooled microbolometer infrared detector with VGA resolution (640 × 480 pixels) and high sensitivity (< 40 mK), enabling precise temperature measurements. Operating at up to 125 Hz in high-speed mode, it captures fast processes without mechanical mirrors. Its uncooled bolometer design offers reliability, cost efficiency, and a minimum detectable spot size of 0.2 mm.

Computational Methodology

The Vienna *ab initio* simulation package (VASP) [41,42] is used to perform the first-principles density functional theory (DFT) calculations. The projector-augmented wave (PAW) potentials are used to describe the ion-electron [43,44] interactions in the systems. The electronic exchange and correlation part of the potential is represented by the Perdew-Burke-Ernzerhof (PBE) [45] generalized gradient approximation (GGA). The Kohn-Sham orbitals are

 This journal is © The Royal Society of Chemistry 20xx

Please do not adjust margins

Please do not adjust margins

expanded using plane wave basis sets with a 500-eV energy cutoff. The conjugate-gradient algorithm is used to relax all structures until the Hellmann-Feynman forces on each atom are less than 0.005 eVÅ^{-1}. For sampling the Brillouin zone (BZ) of Cr_2Te_3, a well-converged Γ −centred Monkhorst-Pack (MP) [46] k-grids of 12 × 12 × 1. We perform *ab initio* Molecular Dynamics (AIMD) analysis at different constant temperature values using the Langevin thermostat within the canonical ensemble (NPT) [47,48] to estimate the magnetic transition temperature as well as the structural transition temperature. The AIMD simulations are run for 2 ps with a time step of 1 fs. For AIMD calculations, we considered the 2 × 2 × 1 supercells for Cr_2Te_3.

Results and Discussion

Structural evaluation

Cr_2Te_3 is a versatile material exhibiting strong tunability of magnetic properties with variations in temperature and thickness, making it suitable for diverse magnetocaloric applications. Bulk Cr_2Te_3 ingots were synthesized by induction or arc melting of stoichiometric Cr and Te in sealed capsules, enabling the preparation of exfoliable material for thin-flake production. Liquid-phase exfoliation was subsequently employed to obtain few-layer flakes with controllable thickness, allowing their integration into flexible substrates and functional coatings for practical device implementation. The induction melted Cr_2Te_3 samples formed a single-phase compound, as confirmed by X-ray diffraction. **Figure 1(a)** revealed a hexagonal Ni-As structure [49] and P3̄ 1c (163) space group with ordered Cr vacancies for both as-cast and exfoliated samples. Cr and Te layers alternate in the layered unit cell, and Cr vacancies can be found in every other metal layer. The major planes were indexed with Topas database. A clear observation of peak shifting to a lower θ value was observed for exfoliated Cr_2Te_3 in comparison to as-cast Cr_2Te_3 (**Figure S2a**). This indicates the separation of layers during exfoliation, introducing solvent ions in between the layers. This may result in possible expansion (loosening) of lattice planes, which is indicated as seen in **Figure 1(a)** resulting broader peaks and shift up to 0.5 ° observed in majority of the exfoliated peaks. The Rietveld Refinement of the XRD is shown in **Figure S2b**. (**Table S(I)** shows the Refinement parameters of Cr_2Te_3.) This is a signature tell that the material has been successfully exfoliated and the strain induces defects in the material [50]. Disappearance of a few peaks are also possible when periodic stacking along c-axis is lost, this happens during prolonged exfoliation of the material. This has also resulted in observing TeO_2 peaks (**Figure 1(a)**) due to surface oxidation of the material *(marked in black)*. The oxide islands thicker than a few tens of nm or oxide covering multiple stacked flakes are detected in this way [51,52]. Exfoliation breaks van-der-Waals bonds and exposes Te atoms at the newly created surface (and creates defects, edge sites, strain). These exposed Te atoms are much more reactive than buried Te and readily react with O_2 (and moisture) in air to form oxidized tellurium species; the thermodynamically stable product is commonly Te (IV) oxide (TeO_2) [52,53]. The experimental details of the material are similar to one of the previous works from our lab, where further details are provided [53]. **Figure 1(b)** shows the EDS composition distribution of exfoliated layers of Cr: 39.55 at% and Te: 60.45 at% present in the compound. We also observe from atomic force microscopic images in **Figure 1(c)** that the exfoliated layers are ~ 22 – 25 nm in thickness. Mechanical exfoliation in liquid solution results in slightly thicker flakes as compared to thin flakes grown in pristine conditions. We adapt this technique of synthesis to produce few-layered Cr_2Te_3 on larger scales for magnetocaloric applications. The HAADF-STEM image of Cr_2Te_3 was examined to determine the atomic arrangement pattern of the Cr and Te atoms. The atomic arrangements revealed two distinct domain orientations, both of which were hexagonal crystal systems, as illustrated in **Figure 1(d)**. The bright dots correspond to Te atoms, which have a larger atomic radius than chromium, with a lattice spacing of 0.206 nm, corresponding to the (1$\bar{1}$0) plane mapped in **Figure 1(a)** during XRD evaluation. The FFT pattern extracted from the HAADF STEM image (**Figure 1(d)**) depicts hexagonal phase formation. Cr_2Te_3 crystallizes in a NiAs-type structure derived from a hexagonal Bravais lattice; however, vacancy ordering and subtle lattice distortions can locally reduce the symmetry to trigonal subgroups such as *P31c* or *P-31c*. In our drop-cast flakes, the presence of multiple domain orientations and overlapping regions yields diffraction patterns consistent with a NiAs-derived lattice, while localized trigonal symmetry cannot be excluded—consistent with previous reports on Cr_2Te_3 [54]. We further confirm the sample composition through XPS analysis. **Figure 1(e)** shows Cr composition with peaks of Cr2p at 574 eV and 584 eV, as well as satellite peaks seen at 577 eV ($2p_{3/2}$) and 586 eV ($2p_{1/2}$), with FWHMs of 3.1 and 3.5, respectively. **Figure 1(f)** shows XPS of Te composition displaying Te3d peaks seen at 587.73 eV for $3d_{1/2}$ and 577.35 for $3d_{5/2}$, which coincide with the $Cr2p_{3/2}$ peak.

Please do not adjust margins

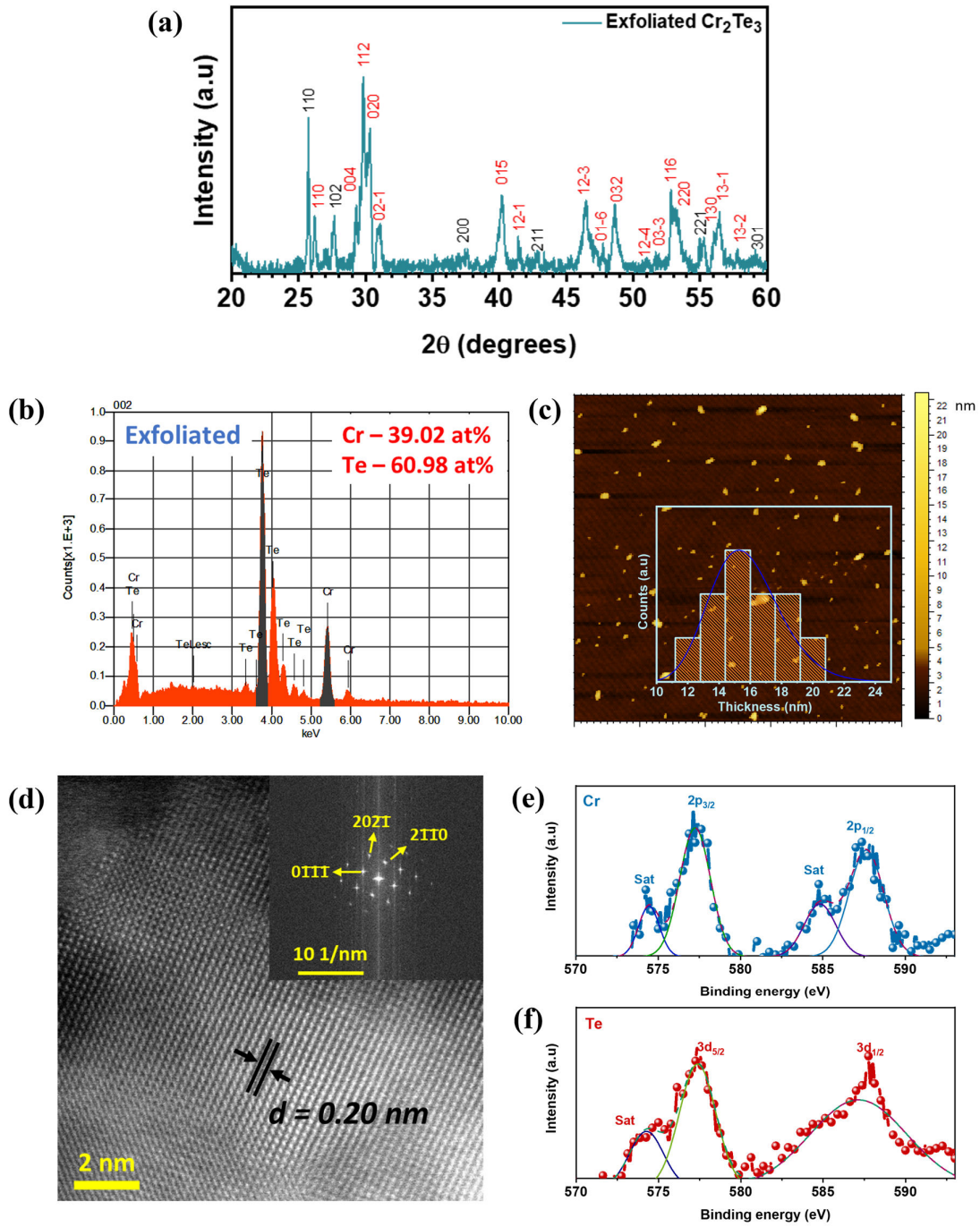

Figure 1. *(a) XRD profile of few-layered exfoliated Cr_2Te_3, (b) EDS of exfoliated Cr_2Te_3, (c) AFM image of the exfoliated sample; inset: line profile of flake distribution, (d) HAADF-STEM image of Cr_2Te_3 with d-spacing of 0.20 nm; inset: FFT pattern derived from (d), XPS spectra of Cr_2Te_3 sample (e) Cr and (f) Te composition.*

Magnetic property discussion

Half-metallicity in Cr compounds is caused by the ordering of the magnetic moment, which is localized at Cr sites and produces magnetism [55]. Cr_2Te_3 is a metallic ferromagnet [56] at lower temperatures. Four Cr sites are vertically oriented, and one layer exhibits modest antiferromagnetic characteristics. Magnetic access with perpendicular magnetic field alignment is provided via the hexagonal *c*-axis. The average values of the Cr localized moment and Te-induced magnetic polarization are found to be antiparallel, with Cr having a moment of 3.30 *μB/Cr* and Te exhibiting a moment of 0.18 *μB/Te* [56]. The addition Cr to magnetic alloys has been used to

This journal is © The Royal Society of Chemistry 20xx

tune the transition temperature for near room temperature (RT) thermal management applications[57]. A 5 % addition of Cr in Fe-Ni-Cr alloy compositions reduced the Curie temperature (T_C) from 438 K to 258 K, enabling use for near RT applications. Cr nanoparticles-based ferrofluid improves thermal contact and accelerates heat exchange compared to bulk systems [58]. To determine the magnetic properties of few-layered Cr_2Te_3, measurements were conducted using a superconducting quantum interference device (SQUID). The temperature-dependent magnetization (M-T) measurements were performed with field-warmed (FW) and field-cooling (FC) conditions under a magnetic field of 1 *T*, as shown in **Figure 2(a)**. The characteristic transformation temperature was determined to be near room temperature in the range of 304 - 308 K. The magnetic transition from ferromagnetic to paramagnetic (FM - PM) transition occurs, which is of particular interest in this study for near-room-temperature magnetic refrigeration. Along with this, isothermal magnetization (M-H) curves at 230 K and 340 K are plotted, respectively, as shown in **Figure 2(b)**. As one can see clearly at 230 K ($T < T_C$), which shows hysteresis as well as FM in nature (black colour). Further, the isothermal magnetization (M-H) curve at 340 K ($T > T_C$) exhibits a linear behaviour with a small slope, which is characteristic of PM, as shown in **Figure 2(b)** (red colour). The plot also observes a secondary phase at high fields of 4 *T*, which does not allow the curves to saturate. This may be due to defects formed during the exfoliation stages of the Cr_2Te_3 sample. The isothermal magnetization curves of Cr_2Te_3 shown in **Figure 2(c)** do not reach complete saturation at an applied field of 4 *T*. This is consistent with intrinsic magnetic behaviour reported in prior studies of Cr_2Te_3, which indicates a combination of itinerant ferromagnetism, magnetic anisotropy, and spin fluctuations. For example, band structure and transport studies reveal that in Cr_2Te_3, the Cr-*3d* / Te-*5p* hybridization leads to magnetic polarization that is not fully aligned at moderate fields [59]. Also, another study shows that reduced density of states (in thinner and bulk forms) and spin fluctuations suppress full alignment of moments under moderate fields [60]. Additionally, magnetocaloric studies in single-crystal Cr_2Te_3 up to 9 *T* indicate that along hard axes, magnetization increases progressively and does not sharply saturate at lower fields, highlighting the role of magneto-crystalline anisotropy[11]. Therefore, the absence of saturation at 4 *T* in our measurements is not unexpected and likely reflects the intrinsic limitations in aligning all spin moments at that field, especially given anisotropies and itinerant contributions. **Figure S3a** shows χ_{hf} values derived for discrete points at 10 K difference (ΔT) from 270 K till 320 K and **Figure S3b** shows a full range of values with fitted curve in the inset. We used $M(H) = M_s(1 - \frac{k}{H^2}) + \chi_{hf} H$; Law of approach to saturation to calculate the chi (χ) value at high field of > 2 *T* (χ_{hf}) for T vs. Ms curve from **Figure 2(a)**. We also estimated the Curie-Weiss fitting for the curve as shown in **Figure S3c**. The estimated Curie temperature from the minimum of the dM/dT curve, $T_C \approx 305$ K also shown in **Figure S3d**.

The most recent research demonstrated that compressive strain can increase MCE in these 2D magnets. Some examples of such compounds include $FeBr_2$ [61], manganites[62], Cr_2O_3[63] and other Cr compounds [58,64,65]. The transition near the critical temperatures has been studied through specific-heat measurements. These experimental results were supported by DFT calculations, which show the second-order magnetic transitions at similar temperatures, as discussed in further sections. Even with these encouraging findings, there is still a lack of basic knowledge regarding how the reduced dimensionality affects the magnetocaloric characteristics of 2D magnets. The saturation magnetization, the T_C, the way the magnetization fluctuates with temperature close to the T_C, and the specific heat capacity are all sensitively dependent on ΔS_M and ΔT. These factors are all qualitatively affected by the lower dimensionality in 2D magnets. To determine the change in magnetic entropy ($|\Delta S_M|$) due to the magnetic field, across the T_C, M-H isotherms at constant temperature were measured from 270 to 320 K within the range of 0 - 4 *T* magnetic field, as shown in **Figure 2(c)**. Magnetocaloric properties of all the investigated Cr_2Te_3 were evaluated using the integral of the isothermal magnetization curve (M-H) as described in **Equation 1**.

$$\Delta S_M(\mathrm{T}, \mathrm{H}_{\mathrm{applied}}) = \int_0^{H_{applied}} \left(\frac{\partial \mathrm{M}}{\partial \mathrm{T}}\right)_H dH \quad (1)$$

Owing to the magnetic phase transition from FM - PM, the maximum $|\Delta S_M|$ is around 1.88 J/kg-K at 304 K. Few studies of thin films, such as GdFeCo, reported a $-\Delta S_M \approx 0.97$ J kg^{-1} K^{-1} for a field change of ±15 kOe around room temperature [66]. $NdCu_2Ge_2$ reported $-\Delta S_M \approx 1.02$ J kg^{-1} K^{-1} for ΔH = 0 – 3 *T*. Temperature ranges include low and near room temperature behaviour depending on composition [67]. $PrCu_2Ge_2$ reported $-\Delta S_M \approx 1.74$ J kg^{-1} K^{-1} ΔH = 0 – 3 *T* (reported in the same work as above). Certain iron-oxide thin films show $-\Delta S_M$ spans 0.13 – 1.87 J·kg^{-1}·K^{-1} for ΔH = 0.5 *T*; specific samples show values comfortably below 1.88 at room temperature [68]. As one can see in **Figure 2(d),** the wide working temperature range directly influences the material's performance in magnetocaloric applications. This is known as cooling capacity or refrigeration capacity (RC), which was calculated to be ~82 J/Kg for few-layered Cr_2Te_3 using **Equation 2** as shown below. Where ΔT_{FWHM} is defined as the temperature difference at the full width at half maxima (FWHM) of ΔS_M curves.

$$RC = \Delta S_M^{Max} \times (\Delta T_{FWHM}) \quad (2)$$

Further calculations of Temperature-averaged entropy change (TEC) were obtained using the following equation [69]

$$TEC(\Delta T_{lift}) = \frac{1}{\Delta T_{lift}} \max_{T_{mid}} \left\{ \int_{T_{mid}-T_{lif}/2}^{T_{mid}+T_{lif}/2} |\Delta S_M(T, \Delta H)| \, dT \right\} \quad (3)$$

Where ΔT_{lift} = 40 K; ΔH = 4 *T* (magnetic field), which was - 0.1325 JKg^{-1}K^{-1}, the negative sign indicates that the entropy decreases as the material becomes more ordered under the applied field (typical for a ferromagnetic transition), therefore $|TEC|$ = 0.1325 JKg^{-1}K^{-1}. Similarly, TEC was computed at 0.5, 1, 2, 3 and 4 *T* as seen in **Figure S4**.

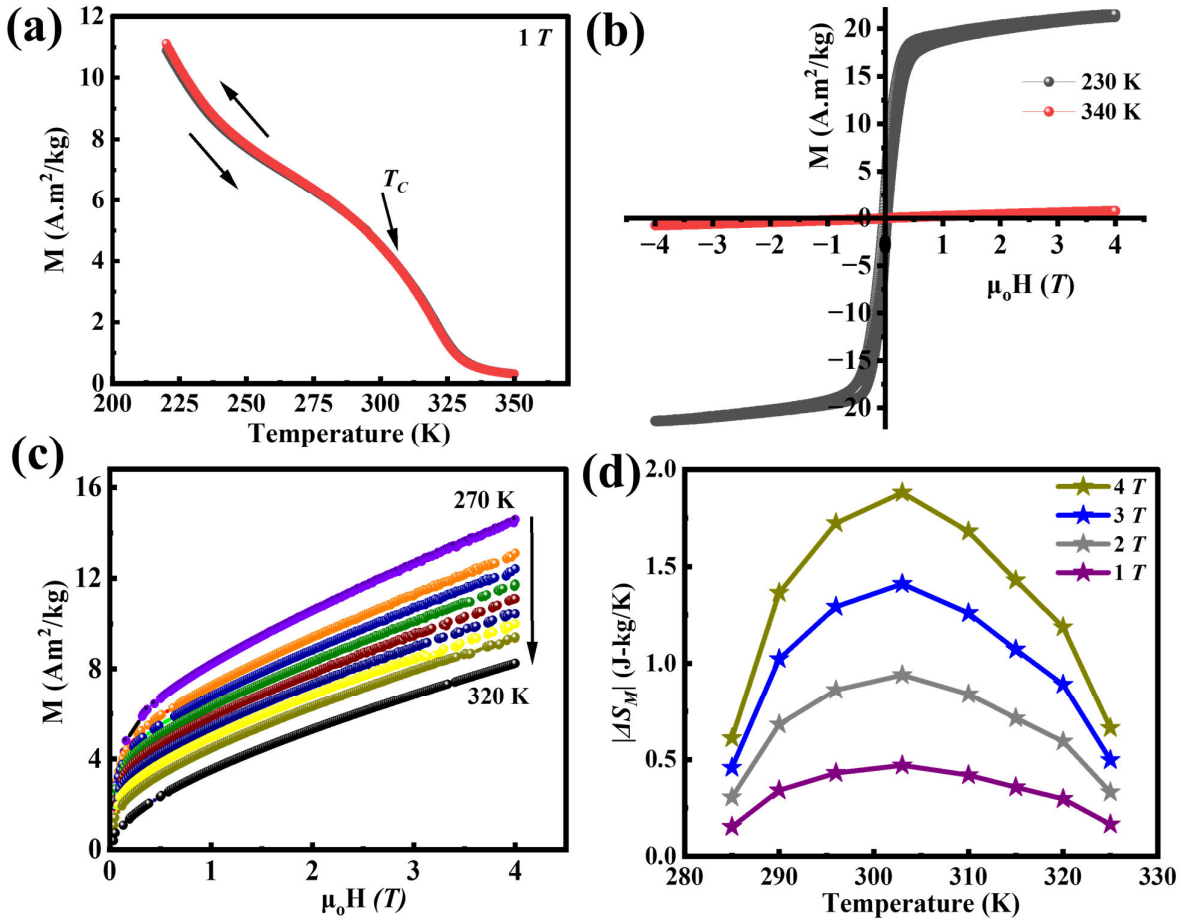

Figure 2. *(a) Magnetization as a function of Temperature (M-T) under the magnetic field of 1 T, (b) M-H curves of few-layered Cr_2Te_3 around 230 and 340 K, (c) M-H curves of few-layered Cr_2Te_3 across the transition temperature (T_c) and (d) Calculated change in magnetic entropy ($|\Delta S_M|$) as a function of temperature at magnetic fields of 1, 2, 3 and 4 T.*

We compare these results with the existing studies involving Cr-based compositions such as Cr_5Te_8, $CrTe_{1-x}Se_x$, CrI_3, CrB_3, Cr-Si-Te, and Cr-Ge-Te, as shown in **Figure 3(a)** [4–10]. Most of them investigated binary telluride shows the magnetocaloric properties below room temperature. Cr_5Te_8 has been extensively studied, and different forms of Cr_5Te_8 exhibit varying values of the $|\Delta S_M|$ in the temperature range of 225-240 K. Monoclinic Cr_5Te_8 shows $|\Delta S_M|$ value of approximated 2.38 J kg^{-1} K^{-1} at 225 K, while trigonal Cr_5Te_8 exhibits maximum $|\Delta S_M|$ at around 240 K [5–7]. These values were measured under an applied magnetic field of 5 *T*, and at temperatures below RT. Researchers have also investigated Cr-Te-X (X = Se, Si, Ge) ternary systems, which show significant changes in magnetocaloric properties. In the Cr-Te-Se ternary system, a $|\Delta S_M|$ value of around 8 J kg^{-1} K^{-1} at 300 K was reported at a magnetic field of 5 *T* by varying the atomic percentages of Te and Se [10]. In the Cr-Si-Te system, adjusting the Si and Te compositions revealed a maximum $|\Delta S_M|$ value of 5.05 J kg^{-1} K^{-1} at 30 K and 5 *T*. Beyond tellurides, magnetocaloric properties have also been explored in chromium-based borides and iodides, albeit at much lower temperatures. CrB_3 exhibits a $|\Delta S_M|$ of approximately 7.2 J kg^{-1} K^{-1} at 33 K and 5 *T*, while CrI_3 shows a $|\Delta S_M|$ of 5.65 J kg^{-1} K^{-1} [8,9] at around 62 K. This study found that few-layered Cr_2Te_3, which are easier to exfoliate on a large scale mechanically, have comparable values of $|\Delta S_M|$ and *RC* of 1.88 J kg^{-1} K^{-1} and 82 J kg^{-1}, respectively, indicating its potential as near room temperature magnetocaloric applications. As summarized above, the values can be seen in **Figure 3(a)**; other TMDCs exhibit magnetocaloric properties at temperatures different from RT and require a higher magnetic field. Similarly, when compared with the existing lower-dimensional structures like 2D and monolayers, the ΔS_M values are higher in lower transition temperatures. **Figure 3(b)** shows a comparison of ΔS_M and T_C of 2D structures. ΔS_M of chromium halides (CrX_3; X: F, Cl, Br, I) ranged between 32.2 to 7.5 J Kg^{-1} $K^{-1,}$ with critical temperature lying below 50 K[27]. These 2D ferromagnets find applications in thermal management units for compact devices. When compared to other 2D magnets, it was discovered that $FeCl_2$, $FeBr_2$, and $RuCl_2$ exhibit higher comprehensive refrigeration capability due to their intrinsic large and high thermal conductivity close to room temperature[28]. Therefore, the engineering of 2D systems becomes a way of exploring novel ferromagnetic compositions close to room temperatures to implement them in effective magnetocaloric applications.

This journal is © The Royal Society of Chemistry 20xx

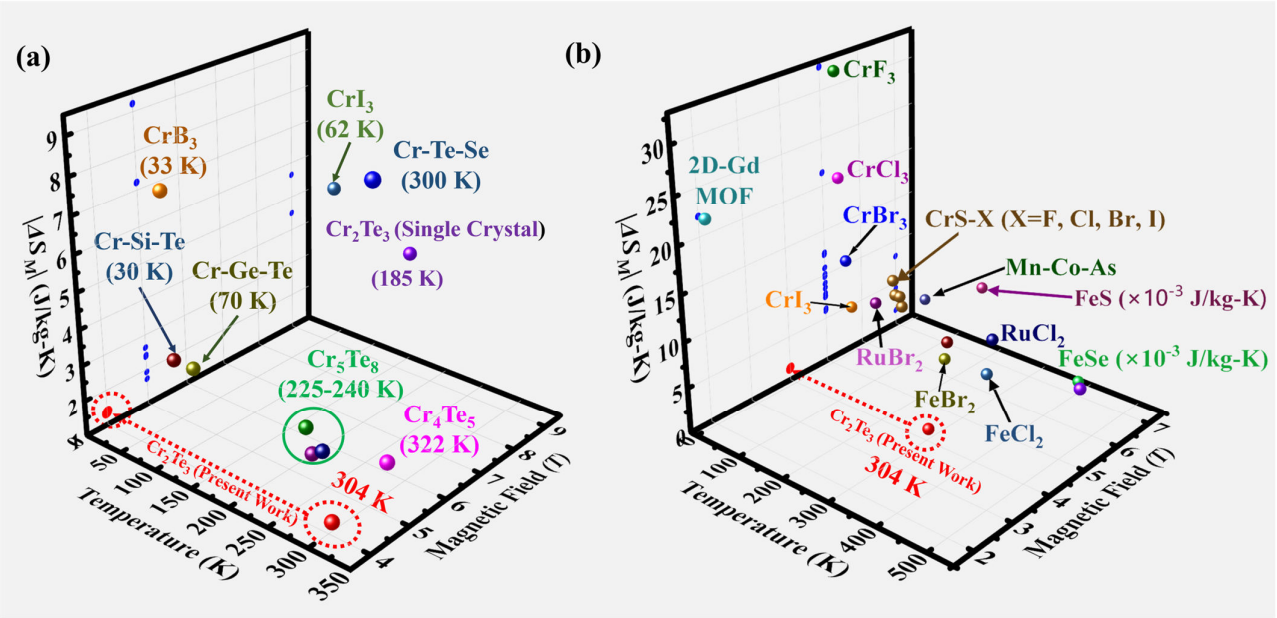

Figure 3. *Magnetocaloric properties of (a) Cr based compositions, including CrB_3 (Red), Cr_5Te_8 (Green circle), Cr_4Te_5 (purple), CrI_3, Cr-Si-Te, Cr-Ge-Te, and Cr-Se-Te in comparison to the present study ($|\Delta S_M|$ ~1.88 J/kg-K) mentioned in red colour* [4–10]. *(b) Comparison with respect to lower-dimensional compositions (2D and monolayers)* [27,28,70–73].

Theoretical studies

First-principles calculations were performed to validate the T_C (Curie Temperature) observed around room temperature for the Cr_2Te_3. The DFT simulated relaxed crystal structure of Cr_2Te_3 (top view) is shown in **Figure 4(a).** The optimized lattice parameters are a = 6.90 Å, b = 6.90 Å, and c = 13.55 Å. There are 14 Cr and 24 Te atoms present in the unit cell of Cr_2Te_3. To understand the magnetic ground state of Cr_2Te_3, we calculate the magnetic ground state energies of Cr_2Te_3 both in ferromagnetic (FM) and antiferromagnetic (AFM) configurations. We found that Cr_2Te_3 exhibits the FM ground state.

For further confirmation, we calculate the spin-projected density of states (DOS) for Cr_2Te_3 under the FM ground state, as shown in **Figure 4(c)**. The d orbitals of Cr and the p orbitals of Te atoms mostly contribute to the total DOS. The majority (spin-up) and minority (spin-down) states are represented in the upper and lower parts of DOS, respectively. The Te atoms have almost the same number of electrons with spin-up and spin-down states, resulting in a negligible net magnetic moment. For Cr atoms, the spin-down states mostly occupy the energy levels above the Fermi level. However, the energy bands for spin-up electrons occupy the energy levels below the Fermi level. This would result in a non-zero cancellation between magnetic moment contributions from spin-up and spin-down states. Therefore, each Cr atom in the unit cell possesses a substantial magnetic moment of 3.392 μ_B, which significantly enhances the system's overall magnetic moment, leading to an FM ground state. Chromium atoms in Cr_2Te_3 carry large local magnetic moments from their partially filled 3d orbitals. These moments couple ferromagnetically. In DFT studies, the Cr 3d states dominate the density of states near the Fermi level in the spin-polarized channels. The projected DOS (pDOS) typically shows strong Cr-3d peaks at and around the Fermi level. One spin channel (majority) is substantially more occupied than the other (minority), producing a clear exchange (spin) splitting of Cr 3d states. That splitting and the imbalance in occupancy are the microscopic origin of the Cr local magnetic moments. Te 5p orbitals hybridize with Cr 3d. In many transition-metal chalcogenides that hybridization allows an indirect exchange channel Cr–(Te)–Cr. Depending on orbital occupancies and bond geometry this channel can favour ferromagnetic or antiferromagnetic coupling. In Cr_2Te_3 the geometry and occupations commonly favour ferromagnetic alignment [60,74,75]. To estimate the magnetic phase transition point, i.e., Curie temperature (T_c) of Cr_2Te_3, we further carried out the AIMD simulations at temperatures T = 100, 150, 180, 200, 220, 250, 270, and 290 K. The magnetic moment variation of Cr_2Te_3 at different temperatures is shown in **Figure 4(d).** The magnitude of the magnetic moment increases with temperature; however, after 250K, there is a sudden decrease in the magnetic moment. This indicates an FM to PM phase transition at 250 K, which is close to the experimentally measured Curie temperature value.

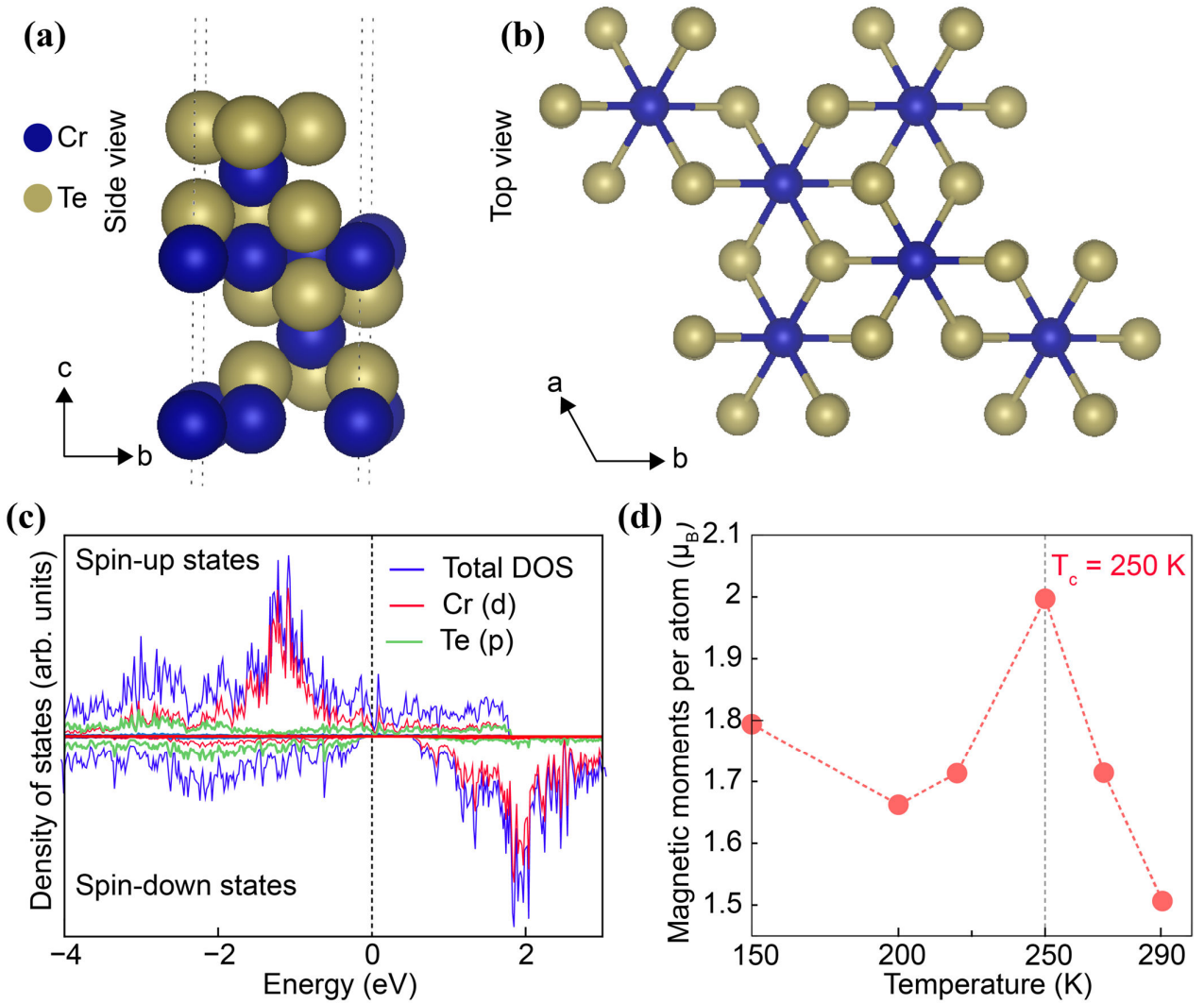

Figure 4. *(a, b) The side and top views of DFT simulated optimized crystal structures of Cr_2Te_3, respectively. (c) The spin-projected DOS for Cr_2Te_3, the upper and lower panels of DOS represent the spin-up and –down states, respectively. (d) The variation of magnetic moment of Cr_2Te_3 at different temperatures.*

Along with the theoretical validation, we have demonstrated the change in temperature under the influence of a magnetic field. It is well known that the magnetic refrigeration cycle consists of adiabatic followed by isothermal processes, while on the application of a magnetic field, two processes occur. Among that, the first step is the temperature of magnetocaloric material increases under adiabatic process and subsequently the material exchanges heat with heat sink which is the second process (isothermal)[76]. In order to demonstrate the increase in temperature with application of magnetic fields we incorporate a thermal imaging technique to show direct MCM property in the ferromagnetic material. Although it may not be ideal for complete cycle but a proof of concept was proposed to observe the temperature difference. The device on application of external magnetic field showed thermal gradient (change in temperature between the marked points), as captured in the thermal imaging camera. The device specifications are mentioned in **Materials and Methods** section as shown in **Figure 5 (a)**. Initially the device was kept in a petri-dish, and low temperature was achieved with the help of liquid nitrogen bed. The device was placed both without and with an external magnetic field in the cold bed, and the associated temperature changes are observed in **Figure 5(b, c)**, respectively. **Figure 5(a)** shows the placement of device directly on the liquid nitrogen bed and the temperature was subsequently raised from -35 °C to + 40 °C using a hot plate. Thermal images were obtained at every 3 °C change and mentioned in **Figure 5(b, c)**. As we observe a transition from FM to PM at T_C ~ 304 K (~ 31 °C), we monitor temperature changes during the transition temperature of 30 ± 5 °C. No particular trap states were observed in the material. Also, the temperature difference between the surrounding liquid nitrogen bed and the material was at temperature gradient of ~ 2 °C consistently. **Video S1** shows heating of the material at transition temperature range from 20 °C to 35 °C (293 K to 308 K). **Figure 5(b) (i – v)** shows the gradual heating process and temperature change in Cr_2Te_3 in the temperature range of 20 °C to 35 °C, where no external magnetic field is applied. The material is also placed with a copper strip, another conducting element that is usually used to fabricate electromagnetic devices. Being a diamagnetic material, the

This journal is © The Royal Society of Chemistry 20xx

behaviour of copper remains similar with and without the application of magnetic fields.

In 2D materials, interfacial thermal resistance (TBR) often limits overall heat transport, especially when the layer rests on a substrate or is stacked with another material. This resistance arises from weak van der Waals coupling and mismatched phonon spectra between the 2D layers and the underlying substrate. Surface defects can sometimes alleviate this issue by improving the physical and vibrational coupling across the interface. The exfoliation introduces vacancies which increase the real contact area, enabling more efficient phonon transmission between the layers. Defects can also suppress flexural phonons that normally scatter strongly at interfaces, allowing more in-plane heat to couple into the substrate. As a result, although intrinsic in-plane conductivity might slightly decline, the effective thermal conductivity of the supported 2D material often increases due to reduced interfacial resistance. This ultrathin nature of the material enables faster heat dissipation and the 2D coating notes better performance in comparison to bulk Cr_2Te_3. The thickness of the material is inversely proportional to heat dissipation. The thicker the material, the larger the inertia requires more energy for heat dissipation. Whereas few-layer/ exfoliated flakes offer a larger surface that has more contact with the surrounding temperature, enabling better and faster thermal dissipation from the object**.**

In the next set of experiments, a small magnetic field was introduced using an NdFeB block magnet (2000 Gauss) under the same experimental conditions. A reversible change in temperature and entropy can be achieved by exposing magnets to an external magnetic field since the magnetic moments will align with the field. **Figure 5(c)** shows the thermal gradient observed from the images, which are obtained at various temperatures in the presence of a magnetic field. While comparing Cr_2Te_3 at 0 sec (20.5 °C (293.5 K)), **Figure 5(b-i) and (c-i)** show no thermal gradient, but as the temperature increases, the difference between the thermal gradients is significant. At 300 sec (23.85 °C (296.85 K)) and 600 sec (29 °C (302 K)) time period (**Figure 5c (ii – iv)**), a large thermal gradient was observed in the presence of an external magnetic field. From the experimental data of temperature-dependent magnetization transitions were observed at T_C in the range of 304-308 K, which led to maximum change in magnetic entropy $|\Delta S_M|$ at around 304 K, as shown in **Figure 2(a)** and **(d)**. The observed increase in temperature upon applying an external magnetic field serves as direct evidence that the material undergoes a magnetocaloric heating cycle. We have presented the temperature variation with and without a magnetic field in **Figures 5(d) and (e)**, respectively. As illustrated in these figures, there is a temperature difference (~2 K) at the marked points of the thermal images (shown in the inset of **Figure 5(d)**) when a magnetic field is applied, at temperatures of 293 K and 305 K. In **Figure 5(f)**, we plot a graph that shows the temperature difference (ΔT) as a function of the temperature (T) from 293 K to 305 K. ΔT represents the difference in temperature at specific points in the thermal images, comparing the results with and without the application of a magnetic field. As the temperature fluctuates within the specified range, this graph illustrates the temperature differences on the surface mapped.

The thermal imaging setup is effective in visualizing localized temperature variations during the magnetocaloric cycle with high spatial and temporal resolution. The system employs a VGA-resolution (640 × 480 pixels) uncooled microbolometer infrared detector, with a smallest detectable spot size (IFOV) of ~0.2 mm per pixel, enabling visualization of local heterogeneities across the sample surface. The thermal noise is below 40 mK, and the low NETD (Noise Equivalent Temperature Difference) ensures sufficient sensitivity to capture the small adiabatic temperature changes (typically in the range of 0.1–2 K) associated with magnetocaloric transitions. Furthermore, the system can operate at frame rates up to 125 Hz in high-speed subframe mode, allowing precise monitoring of transient temperature responses during rapid field cycling.

Quantitative correlation between thermal imaging data and entropy change values derived from isothermal magnetization measurements is feasible by combining the measured adiabatic temperature change (ΔT_{ad}) with independently determined specific heat capacity (Cp) using the thermodynamic relation $\Delta S \approx Cp \cdot (\Delta T_{ad}/T)$. However, it should be noted that our prototype measurements were performed at room temperature under open atmospheric conditions, rather than under strictly adiabatic conditions. Consequently, non-adiabatic heat losses through convection, radiation, and thermal conduction to the sample holder likely led to an underestimation of the true ΔT_{ad} and introduced discrepancies relative to entropy values derived from magnetization. Despite this limitation, the thermal imaging results still provide reliable spatial visualization of localized heating and cooling and allow a semi-quantitative comparison with Maxwell-relation-based entropy change measurements.

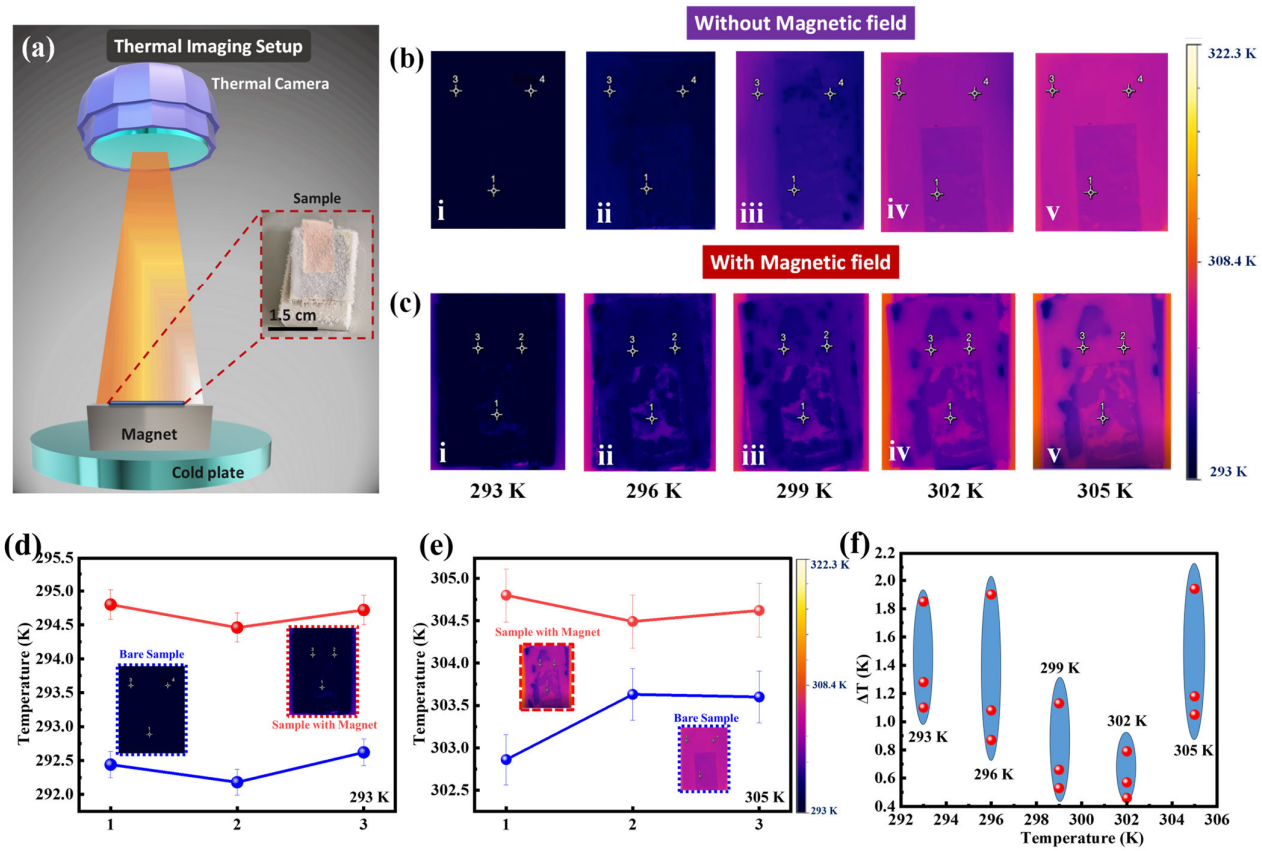

Figure 5. *(a) Thermal imaging camera setup, (b) Thermal images of few-layered Cr_2Te_3 coating without any external magnetic field and (c) Thermal images of Cr_2Te_3 with external magnetic field during gradual heating, (d, e) Temperature change between with and without magnetic field at 293 K and 305 K and (f) ΔT (change in temperature between marked point of thermal images) versus T curve at various temperature (293 to 305 K).*

On application of an external magnetic field, we were able to visualize the clustered areas on the Cr_2Te_3 coating surface through thermal imaging. The tendency to form intrinsic inhomogeneous states is observed due to ordered magnetic clusters or magnetic polarons. It has been previously observed in ferromagnetic samples such as EuB_6 [77] and magnetites [78]. Previous studies observed that cluster formation was more prevalent at the critical temperature (T_C), and the magnetic polarons were imaged with the help of a scanning tunnelling microscope (STM) in these studies [77,78]. Similar cluster formation was observed in our few-layered Cr_2Te_3 on application of external magnetic fields, as compared to images without the exposure to fields. At these points, a drastic reduction in resistance at finite magnetic fields and magnetic phase separation are observed. The suggestive magnetic clusters are strongly field-dependent and affect the temperature gradient as seen in the thermal images. With higher external fields, the cluster network's magnetic moments align more with the direction of the field and combine with the nearby paramagnetic spins. The external magnetic field contributes to the heat capacity, which in turn results in the entropy change in the material at adiabatic conditions.

A potential application of this property of the material can be utilized as a heat sink on existing printed circuit boards (PCBs) [79–81]. The electric circuitry boards with built-in cooling systems have a copper coating or parallel copper plates to minimize localized heating of the circuit components. The copper trace thickness is provided as an impedance path for current flow. PCB management units are focusing on reducing internal heat dissipation, which can help manage these thermal hotspots. A coating of the exfoliated Cr_2Te_3 coatings can be proposed to replace the existing copper metallic coating due to its faster cooling rate on application/presence of external magnetic fields. The thermal resistance of the heat sink materials is often calculated using the following formula:

$$R_{th} = T_1\text{-}T_2/\ P = \Delta\ T/\ P\ (°C/W) \quad (4)$$

where *ΔT* stands for the temperature gradient and P for heat flow. The higher the thermal resistance, the tougher the heat flow; therefore, thinner materials are preferred. The MCM property of cooling on application of an external magnetic field can thus be applied on a large scale for PCB and other electronic circuitry boards.

Conclusions

In summary, the magnetocaloric effect of few-layered Cr_2Te_3 has been investigated in detail for room temperature applications. An integrative analysis of experimental and theoretical studies was performed. The structural characterization, which includes XRD, SEM, AFM, HR-TEM, and XPS, confirms the hexagonal Cr_2Te_3 compound. Magnetic properties have been studied using SQUID (M-

This journal is © The Royal Society of Chemistry 20xx

Please do not adjust margins

T and M-H curves). M-T curves confirm FM - PM transition around room temperature ~ 304 - 308 K, which is an interesting aspect for the current study. Few-layered Cr_2Te_3 exhibits a significant entropy change *(|ΔS_M|)* of around 1.88 J/kg-K at 4 *T* and an *RC* of approximately 82 J/kg due to a wide range of working temperature. Furthermore, we have worked on a prototype to visualize part of the magnetocaloric cycle for the MCE exfoliated Cr_2Te_3 coating with the help of a thermal imaging setup. The DFT studies indicated that the lattice parameter of the relaxed structure changes with temperature, confirming the structural transformation temperature. Additionally, T_C was also calculated considering the FM ground state of the investigated alloys. The DOS calculations confirmed that the magnetic contribution mainly comes from Cr atoms, for the concentration studied. As the atomic positions change with temperature, which leads to a change in magnetic moment, thus magnetic moment is calculated at the transition temperature.

Author contributions

NT and CCG - Conceptualization, Data curation, Formal analysis Investigation, Writing – original draft, Methodology, Writing – original draft, Writing – review & editing; SM - Software, Validation, Visualization, Writing – original draft; PP, ST and VC – Resources, Writing – review & editing; AKS and CST - Funding acquisition, Project administration, Resources, Supervision.

Conflicts of interest

There are no conflicts to declare.

Data availability

The data supporting this article have been included as part of the Supplementary Information.

Acknowledgements

C.S.T acknowledges Core research grant of SERB, India, STARS projects by MHRD-India, DAE Young Scientist Research Award (DAEYSRA), and the AOARD (Asian Office of Aerospace Research and Development) grant no. FA2386-21-1-4014, and Naval research board for funding support. S. T. acknowledges the support from the U. S. Department of Energy (Grant no.: DE-FG02-06ER46291)

References

[1] Q. Cao, F. Grote, M. Humann, S. Eigler, Emerging field of few-layered intercalated 2D materials, Nanoscale Adv 3 (2021) 963–982. https://doi.org/10.1039/d0na00987c.

[2] A. Apte, A. Krishnamoorthy, J.A. Hachtel, S. Susarla, J.C. Idrobo, A. Nakano, R.K. Kalia, P. Vashishta, C.S. Tiwary, P.M. Ajayan, Telluride-Based Atomically Thin Layers of Ternary Two-Dimensional Transition Metal Dichalcogenide Alloys, Chem. Mat. 30 (2018) 7262–7268. https://doi.org/10.1021/acs.chemmater.8b03444.

[3] S. Siddique, C. Chowde Gowda, S. Demiss, R. Tromer, S. Paul, K.K. Sadasivuni, E.F. Olu, A. Chandra, V. Kochat, D.S. Galvão, P. Kumbhakar, R. Mishra, P.M. Ajayan, C. Sekhar Tiwary, Emerging Two-dimensional tellurides, Materials Today 51 (2021) 402–426. https://doi.org/10.1016/j.mattod.2021.08.008.

[4] L.Z. Zhang, A.L. Zhang, X. De He, X.W. Ben, Q.L. Xiao, W.L. Lu, F. Chen, Z. Feng, S. Cao, J. Zhang, J.Y. Ge, Critical behavior and magnetocaloric effect of the quasi-two-dimensional room-temperature ferromagnet Cr_4Te_5, Phys Rev B 101 (2020) 1–8. https://doi.org/10.1103/PhysRevB.101.214413.

[5] X.H. Luo, W.J. Ren, Z.D. Zhang, Magnetic properties and magnetocaloric effect of a trigonal Te-rich Cr_5Te_8 single crystal, J Magn Magn Mater 445 (2018) 37–43. https://doi.org/10.1016/j.jmmm.2017.08.078.

[6] Y. Liu, M. Abeykoon, E. Stavitski, K. Attenkofer, C. Petrovic, Magnetic anisotropy and entropy change in trigonal Cr_5Te_8, Phys Rev B 100 (2019) 1–7. https://doi.org/10.1103/PhysRevB.100.245114.

[7] X. Zhang, T. Yu, Q. Xue, M. Lei, R. Jiao, Critical behavior and magnetocaloric effect in monoclinic Cr_5Te_8, J Alloys Compd 750 (2018) 798–803. https://doi.org/10.1016/j.jallcom.2018.03.318.

[8] X. Yu, X. Zhang, Q. Shi, S. Tian, H. Lei, K. Xu, H. Hosono, Large magnetocaloric effect in van der Waals crystal $CrBr_3$, Front Phys (Beijing) 14 (2019) 6–10. https://doi.org/10.1007/s11467-019-0883-6.

[9] Y. Liu, C. Petrovic, Anisotropic magnetocaloric effect in single crystals of CrI_3, Phys Rev B 97 (2018) 174418. https://doi.org/10.1103/PhysRevB.97.174418.

[10] M.K. Hamad, I.C. Nlebedim, Y. Maswadeh, R. Hamad, K.A. Ziq, Room temperature magnetocaloric effect in $CrTe_{1-x}Se_x$ alloys, Eur Phys J Plus 137 (2022) 1259. https://doi.org/10.1140/epjp/s13360-022-03487-9.

[11] A. Goswami, N. Ng, A.M. Abeykoon, E. Yakubu, S. Guchhait, High Magnetic Anisotropy and Magnetocaloric Effects in Single-Crystal Cr_2Te_3, ACS Appl Electron Mater 6 (2024) 4043–4056. https://doi.org/10.1021/acsaelm.4c00009.

[12] I.H. Lee, B.K. Choi, H.J. Kim, M.J. Kim, H.Y. Jeong, J.H. Lee, S.Y. Park, Y. Jo, C. Lee, J.W. Choi, S.W. Cho, S. Lee, Y. Kim, B.H. Kim, K.J. Lee, J.E. Heo, S.H. Chang, F. Li, B.L. Chittari, J. Jung, Y.J. Chang, Modulating Curie Temperature and Magnetic Anisotropy in Nanoscale-Layered Cr_2Te_3Films:

Please do not adjust margins

Please do not adjust margins

Implications for Room-Temperature Spintronics, ACS Appl Nano Mater 4 (2021) 4810–4819. https://doi.org/10.1021/acsanm.1c00391.

[13] Y. Zhong, C. Peng, H. Huang, D. Guan, J. Hwang, K.H. Hsu, Y. Hu, C. Jia, B. Moritz, D. Lu, J.S. Lee, J.F. Jia, T.P. Devereaux, S.K. Mo, Z.X. Shen, From Stoner to local moment magnetism in atomically thin Cr_2Te_3, Nat Commun 14 (2023) 1–7. https://doi.org/10.1038/s41467-023-40997-1.

[14] J. Zhong, M. Wang, T. Liu, Y. Zhao, X. Xu, S. Zhou, J. Han, L. Gan, T. Zhai, Strain-sensitive ferromagnetic two-dimensional Cr_2Te_3, Nano Res 15 (2022) 1254–1259. https://doi.org/10.1007/s12274-021-3633-3.

[15] H. Chi, Y. Ou, T.B. Eldred, W. Gao, S. Kwon, J. Murray, M. Dreyer, R.E. Butera, A.C. Foucher, H. Ambaye, J. Keum, A.T. Greenberg, Y. Liu, M.R. Neupane, G.J. de Coster, O.A. Vail, P.J. Taylor, P.A. Folkes, C. Rong, G. Yin, R.K. Lake, F.M. Ross, V. Lauter, D. Heiman, J.S. Moodera, Strain-tunable Berry curvature in quasi-two-dimensional chromium telluride, Nat Commun 14 (2023). https://doi.org/10.1038/s41467-023-38995-4.

[16] O. Gutfleisch, M.A. Willard, E. Brück, C.H. Chen, S.G. Sankar, J.P. Liu, Magnetic materials and devices for the 21st century: Stronger, lighter, and more energy efficient, Advanced Materials 23 (2011) 821–842. https://doi.org/10.1002/adma.201002180.

[17] T. Gottschall, K.P. Skokov, M. Fries, A. Taubel, I. Radulov, F. Scheibel, D. Benke, S. Riegg, O. Gutfleisch, Making a Cool Choice: The Materials Library of Magnetic Refrigeration, Adv Energy Mater 9 (2019). https://doi.org/10.1002/aenm.201901322.

[18] K.A. Gschneidner, V.K. Pecharsky, Magnetocaloric Materials, Annu. Rev. Mater. Sci. (2000) 387–429. https://doi.org/10.1146/annurev.matsci.30.1.387.

[19] D. Huang, T. Ma, D.E. Brown, S.H. Lapidus, Y. Ren, J. Gao, Nanoscale Phase Separation and Large Refrigerant Capacity in Magnetocaloric Material LaFe11.5Si1.5, Chemistry of Materials 33 (2021) 2837–2846. https://doi.org/10.1021/acs.chemmater.0c04913.

[20] Q.Y. Xu, K.M. Gu, X.L. Liang, G. Ni, Z.M. Wang, H. Sang, Y.W. Du, Magnetic entropy change in $La_{0.54}Ca_{0.32}MnG_{3-\delta}$, J Appl Phys 90 (2001) 524–526. https://doi.org/10.1063/1.1379047.

[21] Y. Sutou, Y. Imano, N. Koeda, T. Omori, R. Kainuma, K. Ishida, K. Oikawa, Magnetic and martensitic transformations of NiMnX(X=In, Sn, Sb) ferromagnetic shape memory alloys, Appl Phys Lett 85 (2004) 4358–4360. https://doi.org/10.1063/1.1808879.

[22] T. Krenke, E. Duman, M. Acet, E.F. Wassermann, X. Moya, L. Manosa, A. Planes, Inverse magnetocaloric effect in ferromagnetic Ni-Mn-Sn alloys, Nat Mater 4 (2005) 450–454. https://doi.org/10.1038/nmat1395.

[23] P.K. Mishra, A. Gautam, H. Singh, S. Panda, N. Mohapatra, A.K. Ganguli, Interplay of Competing Magnetic Interactions in Noncentrosymmetric Nd_3Te_4 for Enhancing the Magnetocaloric Properties, Chemistry of Materials (2024). https://doi.org/10.1021/acs.chemmater.4c00453.

[24] A. Smith, C.R.H. Bahl, R. Bjork, K. Engelbrecht, K.K. Nielsen, N. Pryds, Materials challenges for high performance magnetocaloric refrigeration devices, Adv Energy Mater 2 (2012) 1288–1318. https://doi.org/10.1002/aenm.201200167.

[25] A. Kitanovski, Energy Applications of Magnetocaloric Materials, Adv Energy Mater 10 (2020). https://doi.org/10.1002/aenm.201903741.

[26] S. Purwar, T.K. Bhowmik, S. Ghorai, S. Thirupathaiah, 3D-Ising-type magnetic interactions stabilized by the extremely large uniaxial magnetocrystalline anisotropy in layered ferromagnetic Cr_2Te_3, Materials Today Physics 46 (2024). https://doi.org/10.1016/j.mtphys.2024.101522.

[27] L. Patra, Y. Quan, B. Liao, Impact of dimensionality on the magnetocaloric effect in two-dimensional magnets, J Appl Phys 136 (2024). https://doi.org/10.1063/5.0218007.

[28] W. Xie, X. Xu, F. Li, G. Zhai, Y. Yue, M. Li, H. Wang, Large magnetocaloric refrigeration performance near room temperature in monolayer transition metal dihalides, Appl Phys Lett 125 (2024). https://doi.org/10.1063/5.0209959.

[29] Y. Liu, C. Petrovic, Anisotropic magnetic entropy change in $Cr_2X_2Te_6$ (X=Si and Ge), Phys Rev Mater 3 (2019). https://doi.org/10.1103/PhysRevMaterials.3.014001.

[30] R. Mondal, R. Mathias, L. V. Bastos, C.C. Gowda, N. Tiwari, H. Singh, C.F. Woellner, C.S. Tiwary, P. Kumbhakar, Two-dimensional chromium telluride-coated 3D-printed architectures for energy harvesting, Nanoscale (2025). https://doi.org/10.1039/d4nr05005c.

[31] A.T. Dinsdale, SGTE DATA FOR PURE ELEMENTS, 1991.

[32] P. Kumbhakar, A. Parui, R.S. Ambekar, M. Mukherjee, S. Siddique, N.M. Pugno, A.K. Singh, C.S. Tiwary, Rain Energy Harvesting Using Atomically Thin Gadolinium Telluride Decorated 3D Printed Nanogenerator, Adv Sustain Syst 6 (2022) 1–10. https://doi.org/10.1002/adsu.202200296.

[33] S. Siddique, C.C. Gowda, R. Tromer, S. Demiss, A.R.S. Gautam, O.E. Femi, P. Kumbhakar, D.S. Galvao, A. Chandra,

 This journal is © The Royal Society of Chemistry 20xx

Please do not adjust margins

Please do not adjust margins

C.S. Tiwary, Scalable Synthesis of Atomically Thin Gallium Telluride Nanosheets for Supercapacitor Applications, ACS Appl Nano Mater 4 (2021) 4829–4838. https://doi.org/10.1021/acsanm.1c00428.

[34] S.D. Negedu, R. Tromer, S. Siddique, C.F. Woellner, F.E. Olu, M. Palit, A.K. Roy, P. Pandey, D.S. Galvao, P. Kumbhakar, C.S. Tiwary, Enhancement in magnetization of two-dimensional cobalt telluride and its magnetic field-assisted photocatalytic activity, Appl Phys A Mater Sci Process 128 (2022). https://doi.org/10.1007/s00339-022-05425-z.

[35] C.C. Gowda, R. Tromer, D. Chandravanshi, P. Pandey, K. Chattopadhyay, D.S. Galvao, C.S. Tiwary, Two-dimensional manganese di-telluride based triboelectric nanogenerator, Nano Energy 117 (2023). https://doi.org/10.1016/j.nanoen.2023.108833.

[36] C.C. Gowda, R. Tromer, P. Pandey, D. Chandravanshi, A. Chandra, K. Chattopadhyay, D.S. Galvao, C.S. Tiwary, Magnetic behavior of two-dimensional manganese telluride, 2D Mater 10 (2023). https://doi.org/10.1088/2053-1583/ace635.

[37] S. Slathia, M. Tripathi, R. Tromer, C.C. Gowda, P. Pandey, D.S. Galvao, A. Dalton, C.S. Tiwary, Thickness dependent nanoscale magnetism in two-dimensional manganese telluride (MnTe), Mater Today Chem 38 (2024). https://doi.org/10.1016/j.mtchem.2024.102134.

[38] H. Cho, M. Heo, K.H. Lee, H. Park, S. Park, J. Park, H.S. Kim, S. il Kim, Electrical and thermal transport properties of Cr2Se3-Cr2Te3 solid-solution alloy system and estimation of optimal thermoelectric properties, J Alloys Compd 1006 (2024). https://doi.org/10.1016/j.jallcom.2024.176241.

[39] C.I. Abilov, M.S. Hasanova, N.T. Huseynova, Physico-chemical properties and thermodynamic functions of alloys of the system InTe–Cr_2Te_3, Mater Chem Phys 241 (2020). https://doi.org/10.1016/j.matchemphys.2019.122341.

[40] K. Ramasamy, D. Mazumdar, R.D. Bennett, A. Gupta, Syntheses and magnetic properties of Cr_2Te_3 and $CuCr_2Te_4$ nanocrystals, Chemical Communications 48 (2012) 5656–5658. https://doi.org/10.1039/c2cc32021e.

[41] G. Kresse, J. Furthmüller, Efficiency of ab-initio total energy calculations for metals and semiconductors using a plane-wave basis set, Comput Mater Sci 6 (1996) 15–50. https://doi.org/10.1016/0927-0256(96)00008-0.

[42] G. Kresse and J Furthmuller, Efficient iterative schemes for ab initio total-energy calculations using a plane-wave basis set, Phys. Rev. B 54 (1996) 11169. https://doi.org/10.1021/acs.jpca.0c01375.

[43] P.E. Blöchl, Projector augmented-wave method, Phys Rev B 50 (1994) 17953–17979. https://doi.org/10.1103/PhysRevB.50.17953.

[44] J.P. Perdew, K. Burke, M. Ernzerhof, Generalized Gradient Approximation Made Simple [Phys. Rev. Lett. 77, 3865 (1996)], Phys Rev Lett 78 (1997) 1396–1396. https://doi.org/10.1103/PhysRevLett.78.1396

[45] D. Joubert, From ultrasoft pseudopotentials to the projector augmented-wave method, Phys Rev B Condens Matter Mater Phys 59 (1999) 1758–1775. https://doi.org/10.1103/PhysRevB.59.1758.

[46] Hendrik J. Monkhorst and James D. Pack, Special points for Brillonin-zone integrations, Phys Rev B 13 (1976). https://doi.org/10.1039/c8ta11250a.

[47] B.L. Holian, D.J. Evans, Shear viscosities away from the melting line: A comparison of equilibrium and nonequilibrium molecular dynamics, J Chem Phys (1983) 5147–5150. https://doi.org/10.1063/1.445384.

[48] W.G. Hoover, A.J.C. Ladd, B. Moran, High-strain-rate plastic flow studied via nonequilibrium molecular dynamics, Phys Rev Lett 48 (1982) 1818–1820. https://doi.org/10.1103/PhysRevLett.48.1818.

[49] D.M. Burn, L.B. Duffy, R. Fujita, S.L. Zhang, A.I. Figueroa, J. Herrero-Martin, G. van der Laan, T. Hesjedal, Cr_2Te_3 Thin Films for Integration in Magnetic Topological Insulator Heterostructures, Sci Rep 9 (2019) 1–10. https://doi.org/10.1038/s41598-019-47265-7.

[50] Y. Yamaguchi, H. Watanabe, Neutron Diffraction Study of Cr_2te_3 Single Crystal, Pergamon Press 16 (1975) 895-897. https://doi.org/10.1016/0038-1098(75)90888-1

[51] D.M. Burn, L.B. Duffy, R. Fujita, S.L. Zhang, A.I. Figueroa, J. Herrero-Martin, G. van der Laan, T. Hesjedal, Cr_2Te_3 Thin Films for Integration in Magnetic Topological Insulator Heterostructures, Sci Rep 9 (2019) 1–10. https://doi.org/10.1038/s41598-019-47265-7.

[52] J. Swanson, S.E. El Jamal, T. Hartman, O.C. Stewart, P. Glaser, A.J. Biacchi, D.V. Henry, A. Liu, S.L. Stoll, Solution Synthesis of $NdTe_3$ Magnetic Nanosheets, Chemistry of Materials 36 (2024) 7056–7068. https://doi.org/10.1021/acs.chemmater.4c01362.

[53] C. Chowde Gowda, A. Kartsev, N. Tiwari, A.A. Safronov, P. Pandey, A.K. Roy, P.M. Ajayan, D.S. Galvão, C.S. Tiwary, Non-thermal magnetic deicing using two-dimensional chromium telluride, J Mater Chem C Mater (2024). https://doi.org/10.1039/d4tc02542c.

Please do not adjust margins

Please do not adjust margins

[54] Q.D. Gibson, D. Wen, H. Lin, M. Zanella, L.M. Daniels, C.M. Robertson, J.B. Claridge, J. Alaria, M.S. Dyer, M.J. Rosseinsky, Control of Polarity in Kagome-NiAs Bismuthides, Angewandte Chemie - International Edition 63 (2024). https://doi.org/10.1002/anie.202403670.

[55] K. Ramasamy, D. Mazumdar, R.D. Bennett, A. Gupta, Syntheses and magnetic properties of Cr_2Te_3 and $CuCr_2Te_4$ nanocrystals, Chemical Communications 48 (2012) 5656–5658. https://doi.org/10.1039/c2cc32021e.

[56] J. Dijkstra, H.H. Weitering, C.F. Van Bruggen, C. Haas, R.A. De Groot, Band-structure calculations, and magnetic and transport properties of ferromagnetic chromium tellurides (CrTe, Cr_3Te_4, Cr_2Te_3), Journal of Physics: Condensed Matter 1 (1989) 9141–9161. https://doi.org/10.1088/0953-8984/1/46/008.

[57] V. Chaudhary, X. Chen, R. V. Ramanujan, Iron and manganese based magnetocaloric materials for near room temperature thermal management, Prog Mater Sci 100 (2019) 64–98. https://doi.org/10.1016/j.pmatsci.2018.09.005.

[58] V. Chaudhary, R. V. Ramanujan, Magnetocaloric Properties of Fe-Ni-Cr Nanoparticles for Active Cooling, Sci Rep 6 (2016). https://doi.org/10.1038/srep35156.

[59] M. Gani, K.A. Shah, S.A. Parah -, T.X. M Zhao, Y.Z. Li, L.L. Zhao, Band-structure calculations, and magnetic and transport properties of ferromagnetic chromium tellurides (CrTe, Cr_3Te_4, Cr_2Te_3), 1989. https://iopscience.iop.org/10.1088/0953-8984/1/46/008

[60] Y. Zhong, C. Peng, H. Huang, D. Guan, J. Hwang, K.H. Hsu, Y. Hu, C. Jia, B. Moritz, D. Lu, J.S. Lee, J.F. Jia, T.P. Devereaux, S.K. Mo, Z.X. Shen, From Stoner to local moment magnetism in atomically thin Cr_2Te_3, Nat Commun 14 (2023) 1–7. https://doi.org/10.1038/s41467-023-40997-1.

[61] N.L. Di, S. Morimoto, A. Ito, Transition from the paramagnetic to the antiferromagnetic state actualized in FeBr2, Journal of Physics Condensed Matter 16 (2004) 3725–3736. https://doi.org/10.1088/0953-8984/16/21/021.

[62] A. Oleaga, A. Salazar, D. Prabhakaran, J.G. Cheng, J.S. Zhou, Critical behavior of the paramagnetic to antiferromagnetic transition in orthorhombic and hexagonal phases of $RMnO_3$ (R=Sm, Tb, Dy, Ho, Er, Tm, Yb, Lu, Y), Phys Rev B Condens Matter Mater Phys 85 (2012). https://doi.org/10.1103/PhysRevB.85.184425.

[63] Y. Shapira, C.C. Becerra, Increase of the Paramagnetic-To-Antiferromagnetic Transition Temperature of Cr_2O_3 by a Magnetic Field, Phy lett. A 59 (1976) 75-76. https://doi.org/10.1016/0375-9601(76)90359-5.

[64] L. Zu, S. Lin, Y. Liu, J.C. Lin, B. Yuan, X.C. Kan, P. Tong, W.H. Song, Y.P. Sun, A first-order antiferromagnetic-paramagnetic transition induced by structural transition in $GeNCr_3$, Appl Phys Lett 108 (2016). https://doi.org/10.1063/1.4940365.

[65] S. Mishra, N. Maity, A.K. Singh, Symmetry-assisted anomalous Hall conductivity in a CrS_2-$CrBr_3$ heterostructure, Phys Rev B 110 (2024). https://doi.org/10.1103/PhysRevB.110.125406.

[66] G.J. Kumar, Z. Guo, L. Gu, J. Feng, K. Kamala Bharathi, K. Wang, Broad table-like magnetocaloric effect in GdFeCo thin-films for room temperature Ericsson-cycle magnetic refrigeration, J Appl Phys 135 (2024). https://doi.org/10.1063/5.0191497.

[67] X. Wang, Y. Ma, Z. Zhang, Structural and Cryogenic Magnetic Properties of the Ternary $RECu_2Ge_2$ (RE = Pr and Nd) Compounds, J Electron Mater 51 (2022) 5664–5669. https://doi.org/10.1007/s11664-022-09808-z.

[68] M. Bohra, P. Gupta, D. Sahadot, A. Annadi, V. Singh, J.F. Bobo, Determination of normal and inverse magnetocaloric effect in iron oxide thin films, Appl Phys A Mater Sci Process 129 (2023). https://doi.org/10.1007/s00339-023-06993-4.

[69] L. Gu, J.K. Galivarapu, Z. Wang, K. Wang, Interface-Induced Conventional and Inverse Magnetocaloric Properties of GdFeCo Thin Films, ACS Appl Electron Mater 7 (2025) 1812–1819. https://doi.org/10.1021/acsaelm.4c02066.

[70] S. Kumar, G.G. Riera, A. Arauzo, J. Hrubý, S. Hill, L. Bogani, J. Rubio-Zuazo, J. Jover, E. Bartolomé, E.C. Sañudo, On-surface magnetocaloric effect for a van der Waals Gd(iii) 2D MOF grown on Si, J Mater Chem A Mater 12 (2024) 6269–6279. https://doi.org/10.1039/d3ta06648g.

[71] Q. Liu, J. Kang, P. Wang, W. Gao, Y. Qi, J. Zhao, X. Jiang, Inverse Magnetocaloric Effect in Altermagnetic 2D Non-van der Waals FeX (X = S and Se) Semiconductors, Adv Funct Mater (2024). https://doi.org/10.1002/adfm.202402080.

[72] G. Zhai, X. Xu, C. Niu, W. Xie, M. Li, X. Lin, H. Wang, Giant magnetocaloric effect in Cr-based two-dimensional materials, Appl Phys Lett 126 (2025). https://doi.org/10.1063/5.0257684.

[73] Q. Liu, Y. Liu, X. Jiang, Y. Qi, J. Gao, J. Zhao, Magnetocaloric effect near room temperature in a freestanding two-dimensional non-van der Waals crystal of MnCoAs, Phys

 This journal is © The Royal Society of Chemistry 20xx

Please do not adjust margins

Please do not adjust margins

Rev B 108 (2023). https://doi.org/10.1103/PhysRevB.108.054427.

[74] L. Zhang, Z. Jiang, Y. Zhang, J. Zhang, A. Wang, M. He, Y.P. Sun, X. Luo, Y. Chai, Magnetic phase diagram of Cr_2Te_3 revisited by ac magnetostrictive coefficient, Appl Phys Lett 127 (2025). https://doi.org/10.1063/5.0271368.

[75] F. Wang, J. Du, F. Sun, R.F. Sabirianov, N. Al-Aqtash, D. Sengupta, H. Zeng, X. Xu, Ferromagnetic Cr_2Te_3 nanorods with ultrahigh coercivity, Nanoscale 10 (2018) 11028–11033. https://doi.org/10.1039/c8nr02272k.

[76] V. Franco, J.S. Blázquez, J.J. Ipus, J.Y. Law, A. Conde, Progress in Materials Science Magnetocaloric effect: From materials research to refrigeration devices, Prog Mater Sci 93 (2018) 112–232. https://doi.org/10.1016/j.pmatsci.2017.10.005.

[77] M. Pohlit, S. Rößler, Y. Ohno, H. Ohno, S. Von Molnár, Z. Fisk, J. Müller, S. Wirth, Evidence for Ferromagnetic Clusters in the Colossal-Magnetoresistance Material EuB_6, Phys Rev Lett 120 (2018). https://doi.org/10.1103/PhysRevLett.120.257201.

[78] J.Z. Sun, L. Krusin-Elbaum, A. Gupta, G. Xiao, S.S.P. Parkin, Does magnetization in thin-film manganates suggest the existence of magnetic clusters?, Appl Phys Lett 69 (1996) 1002–1004. https://doi.org/10.1063/1.117966.

[79] L. Coppola, B. Agostini, R. Schmidt, R. Faria Barcelos, Influence of connections as boundary conditions for the thermal design of PCB traces, IEEE International Symposium on Industrial Electronics (2010) 884–888. https://doi.org/10.1109/ISIE.2010.5637243.

[80] K. Chen, I. Hsu, C. Lee, Chip-package-PCB thermal co-design for hot spot analysis in SoC, 2012 IEEE Electrical Design of Advanced Packaging and Systems Symposium, EDAPS 2012 (2012) 215–218. https://doi.org/10.1109/EDAPS.2012.6469401.

[81] J.A. Cooley, M.K. Horton, E.E. Levin, S.H. Lapidus, K.A. Persson, R. Seshadri, From Waste-Heat Recovery to Refrigeration: Compositional Tuning of Magnetocaloric $Mn_{1+x}Sb$, Chemistry of Materials 32 (2020) 1243–1249. https://doi.org/10.1021/acs.chemmater.9b04643.

This journal is © The Royal Society of Chemistry 20xx

Please do not adjust margins